

RESEARCH ARTICLE | FEBRUARY 09 2010

Drift-resistive-inertial ballooning modes in quasihelical stellarators

T. Rafiq; C. C. Hegna; J. D. Callen; A. H. Kritz



Phys. Plasmas 17, 022502 (2010)

<https://doi.org/10.1063/1.3291061>



Articles You May Be Interested In

Dissipative trapped-electron instability in quasihelically symmetric stellarators

Phys. Plasmas (June 2006)

Local ideal magnetohydrodynamic stability of a quasihelically symmetric stellarator

Phys. Plasmas (October 1996)

Development of drift-resistive-inertial ballooning transport model for tokamak edge plasmas

Phys. Plasmas (August 2010)



Physics of Plasmas

Special Topics Open
for Submissions

[Learn More](#)

Drift-resistive-inertial ballooning modes in quasihelical stellarators

T. Rafiq,¹ C. C. Hegna,² J. D. Callen,² and A. H. Kritz¹

¹*Department of Physics, Lehigh University, Bethlehem, Pennsylvania 18015, USA*

²*Department of Engineering Physics and Department of Physics, University of Wisconsin, Madison, Wisconsin 53706, USA*

(Received 13 August 2009; accepted 18 December 2009; published online 9 February 2010)

A linear stability theory of nonideal magnetohydrodynamic (MHD) ballooning modes is investigated using a two fluid model for electron-ion plasmas. Drift-resistive-inertial ballooning mode eigenvalues and eigenfunctions are calculated for a variety of equilibria including axisymmetric shifted circular geometry ($\hat{s}-\alpha$ model) as well as for three dimensional configurations relevant for the Helically Symmetric Stellarator (HSX) [F. S. B. Anderson, A. F. Almagri, D. T. Anderson, *et al.*, *Fusion Technology* **27**, 273 (1995)]. For typical HSX parameters, characteristic ballooning mode growth rates exceed the electron collision frequency. In this regime, electron inertial effects dominate plasma resistivity and produce an instability whose growth rate scales with the electromagnetic skin depth. However, as plasma β is increased, the resistive and inertial effects become unimportant. Under these conditions, the mode is completely stabilized by drift frequency effects, which dominate resistivity and inertia. Numerical results indicate that in the absence of drift effects, the resistive-inertial MHD modes are purely growing and persist in regimes where ideal MHD ballooning modes are stable. It is found that the magnitudes of the linear growth rates are not sensitive to the addition of a mirror term to the magnetic spectrum that spoils the quasihelical symmetry of the configuration. The eigenvalues and eigenvectors in the strong ballooning approximation are used together with a quasilinear mixing length estimate to determine particle flux and particle diffusivity. The particle diffusivity increases with rising density gradient and collisionality in a plasma with a low electron temperature. This increase in transport is consistent with the increase observed in the edge region of HSX plasmas. The magnitude of the particle diffusivity is computed to be in the range from 5 to 10 m²/s, which is consistent with the experimental measured particle diffusivity at the edge of HSX plasmas. © 2010 American Institute of Physics. [doi:10.1063/1.3291061]

I. INTRODUCTION

Unstable resistive ballooning modes (RBMs) may play an important role in producing edge plasma fluctuations and anomalous transport in tokamaks and stellarators. Resistive modes are normally expected to be unstable in the plasma edge region in tokamak discharges. The RBMs grow in the edge region because of the typically low electron temperature and moderately high density. RBMs have been studied in axisymmetric tokamaks using linear¹⁻⁸ and nonlinear theories.⁹⁻¹¹ However, the study of RBMs in fully three-dimensional stellarator geometries is more limited.¹²⁻¹⁷

Stellarator geometry makes the problem more difficult because of its complicated three-dimensional structure and the related high resolution required in a numerical treatment. In Ref. 14, RBMs were studied in general geometry based on the linearized equations of motion of resistive magnetohydrodynamics (RMHD). In that study, a multiple-length-scale expansion technique was used based on a small resistivity and growth rate expansion. RMHD equations computed in Ref. 16 for the Wendelstein 7-X (W7-X) configuration are compared and contrasted with the results with W7-AS using the Corraera–Restrepo formulation given in Ref. 14. In W7-X equilibria, it was shown that the destabilizing effect of resistivity is largely compensated by the stabilizing contribution of plasma compressibility. This behavior persists up to the

ideal marginal limit. For W7-AS, where larger resistive effects are observed due to higher resistivity and lower plasma pressure, the situation is different. A general theory applicable to three-dimensional (3D) configurations that avoids the usual restrictive assumptions ($\omega \gg \omega_{*en} \gg \omega_\kappa$, where ω is the mode frequency, ω_κ is the curvature drift frequency, and ω_{*en} is the electron diamagnetic drift frequency, and zero electron inertia) is not available. It is important to develop a model for the stability limit of RBMs and their dependence on the equilibrium configuration in order to predict the edge transport in both tokamaks and stellarators. This paper is focused on developing an appropriate model for RBMs.

In this work, a nonideal MHD ballooning mode model is derived that allows prediction of particle transport in the edge region of quasihelically symmetric stellarators (QHSS) with an emphasis on configurations of interest to HSX. In the presence of nonideal effects, ballooning instabilities can be produced at plasma β levels far below the critical β required for an ideal ballooning instability. Electron inertia, diamagnetic effects, parallel ion dynamics, transverse particle diffusion, and perpendicular gyroviscous stress terms are included in the calculations. Temperature perturbations, equilibrium temperature gradients, and electron trapping are ignored in order to simplify the analysis. For parameters of interest for the Helically Symmetric Experiment (HSX),¹⁸ characteristic growth rates exceed the electron collision frequency. In this

regime, electron inertia effects can dominate plasma resistivity and produce an instability whose growth rate scales with the electromagnetic skin depth.

In this paper, a unified theory of RBM and inertial ballooning modes is developed. The theory can be applied to the $k_y \leq 1/\text{cm}$ fluctuations and to the anomalous plasma transport observed in HSX near $r/\bar{a} \approx 0.7$, where \bar{a} is a minor radius and $T_e \approx 100$ eV.¹⁹ The resistive-inertial ballooning mode eigenvalues and eigenfunctions are numerically evaluated for axisymmetric shifted circular geometry ($\hat{s}-\alpha$ model) as well as 3D stellarator equilibria.

The organization of this paper is as follows. In Sec. II, linearized ballooning equations are derived from Ohm's law, vorticity, continuity, and total parallel momentum equations. In Sec. III, the resistive-inertial MHD (RIMHD), ideal MHD (IMHD), and drift-resistive-inertial ballooning mode (DRIBM) eigenvalue equations are developed and numerically evaluated for $\hat{s}-\alpha$ geometry. The RIMHD modes in the electrostatic limit are calculated for a 3D QHS equilibrium. The results for a QHS device are compared and contrasted with those for a magnetic configuration that spoils the helical symmetry by adding mirror terms to the magnetic spectrum (for details, see Refs. 20 and 21). In Sec. IV, the particle diffusivity in the strong ballooning limit is presented by using eigenvalues and eigenvectors together with a quasilinear estimate. In Sec. V a discussion of the results and conclusions are presented.

II. DISSIPATIVE DRIFT BALLOONING EQUATIONS

The reduced Braginskii fluid equations are used for a four-field model of drift RBMs with high mode numbers (for details, see Refs. 22 and 23). The equations for the parallel component of generalized Ohm's law, vorticity, electron continuity, and total parallel momentum can be written in the following form:

$$E_{\parallel} + T_e \nabla_{\parallel} n_e - \eta j_{\parallel} = \frac{m_e}{e^2 n_e} \frac{\partial j_{\parallel}}{\partial t}, \quad (1)$$

$$\nabla \cdot n(\mathbf{v}_{pi} + \mathbf{v}_{mi}) + \nabla \cdot n(\mathbf{v}_{Di} - \mathbf{v}_{De}) + \nabla \cdot (n\mathbf{v}_{pe}) + \frac{1}{e} \nabla_{\parallel} j_{\parallel} = 0, \quad (2)$$

$$\frac{\partial n}{\partial t} + \nabla \cdot n(\mathbf{v}_E + \mathbf{v}_{De}) + \nabla \cdot n(\mathbf{v}_{pe} + \mathbf{v}_{\eta}) + \nabla \cdot (n\mathbf{v}_{\parallel e}) = 0, \quad (3)$$

$$m_i n \left(\frac{\partial}{\partial t} \right) v_{i\parallel} = -\hat{\mathbf{b}} \cdot \nabla (p_i + p_e) - \hat{\mathbf{b}} \cdot (\nabla \cdot \boldsymbol{\pi}_i), \quad (4)$$

where

$$E_{\parallel} = -\nabla_{\parallel} \phi - \frac{1}{c} \frac{\partial A_{\parallel}}{\partial t}, \quad (5)$$

$$\mathbf{v}_E = -\frac{c}{B} \nabla \phi \times \hat{\mathbf{b}}, \quad (6)$$

$$\mathbf{v}_{Dj} = -\frac{c}{q_j B n} \nabla p_j \times \hat{\mathbf{b}}, \quad (7)$$

$$\mathbf{v}_{\pi i} = -\frac{c}{e B n} \nabla \cdot \boldsymbol{\pi}_i \times \hat{\mathbf{b}}, \quad (8)$$

$$\mathbf{v}_{\eta} = \frac{c}{e B n} \mathbf{R} \times \hat{\mathbf{b}}, \quad (9)$$

and

$$\mathbf{v}_{pj} = \frac{1}{\omega_{ci}} \left(\frac{\partial}{\partial t} + \mathbf{v}_j \cdot \nabla \right) \mathbf{v}_j \times \hat{\mathbf{b}}. \quad (10)$$

Here $\hat{\mathbf{b}} = \mathbf{B}/|B|$ is the unit vector along the magnetic field line, $\omega_{ci} = eB_0/m_i c$ is the ion cyclotron frequency evaluated at the magnetic axis, $\mathbf{j}_{\parallel} = en(v_{\parallel i} - v_{\parallel e})$ is the plasma current parallel to the magnetic field, ϕ is the electrostatic potential, $p = n(T_i + T_e)$ is the isotropic pressure, T_j is the equilibrium temperature of species j (which is assumed to be constant), and $\boldsymbol{\pi}_i$ is the anisotropic ion stress tensor. The velocity $\mathbf{v}_{\pi i}$ is due to the stress tensor $\boldsymbol{\pi}$, which contains both viscous and finite Larmor radius (FLR) contributions, (cf. p. 20 in Ref. 4) and \mathbf{R} denotes the frictional force. The electron stress tensor is neglected. Electron and ion densities are both denoted by n . To the lowest order ($\omega \ll \omega_{ci}$), $\mathbf{v}_j = \mathbf{v}_E + \mathbf{v}_{Dj}$ is substituted into the above polarization flow \mathbf{v}_{pj} for species j . However, the total ion and electron velocities used in Eqs. (2) and (3) are

$$\mathbf{v}_i = \mathbf{v}_E + \mathbf{v}_{Di} + \mathbf{v}_{pi} + \mathbf{v}_{\pi i} + \mathbf{v}_{\parallel i}, \quad (11)$$

$$\mathbf{v}_e = \mathbf{v}_E + \mathbf{v}_{De} + \mathbf{v}_{pe} + \mathbf{v}_{\eta} + \mathbf{v}_{\parallel e}. \quad (12)$$

Note that the perpendicular electric field in Eq. (6) is electrostatic in the limit of low β . Electromagnetic effects, other than Ohm's law, are included in these model equations through the parallel gradient $\nabla_{\parallel} = \hat{\mathbf{b}} \cdot \nabla = \hat{\mathbf{b}}^{(0)} \cdot \nabla + \hat{\mathbf{b}}^{(1)} \cdot \nabla$, where $\hat{\mathbf{b}}^{(0)}$ is the direction of the unperturbed magnetic field, and $\hat{\mathbf{b}}^{(1)} = \nabla \times \tilde{\mathbf{A}}_{\parallel} / B = \nabla \tilde{\mathbf{A}}_{\parallel} \times \hat{\mathbf{e}}_{\parallel} / B$ is the magnetic perturbation associated with field line bending, A_{\parallel} . It follows that, when $\hat{\mathbf{b}}^{(1)} \cdot \nabla$ operates on variable the equilibrium S_0 , it has the linearized form, $-iS_0 \omega_{*s} \hat{A}_{\parallel}$, where $\omega_{*s} = -(cT_e/eB) \mathbf{k} \cdot \hat{\mathbf{e}}_{\parallel} \times \nabla \ln S_0$.

When quasineutrality is assumed, $n = n_e = n_i$, Ampère's law reduces to

$$\nabla_{\perp}^2 \tilde{A}_{\parallel} = -\frac{4\pi}{c} \tilde{j}_{\parallel}. \quad (13)$$

Equations (1)–(4) can be written, using $\nabla_{\perp} = ik_{\perp}$, $\partial/\partial t = -i\omega$, in the following linearized form in $\omega \sim \omega_s \sim \omega_{*j} \sim \omega_{\eta}$ maximal ordering,

$$(\omega - \omega_{*en} + \omega H + ic^2 k_{\perp}^2 \eta_{\parallel} / 4\pi) \hat{\Psi} = -ic_s \nabla_{\parallel}^{(0)} (\hat{\Phi} - \hat{n}), \quad (14)$$

$$\omega k_{\perp}^2 \rho_i^2 (\hat{n} + \tau \hat{\Phi}) = \omega_{\kappa} \hat{n} + k_{\perp}^2 \rho_e^2 (\omega - \omega_{*en}) \hat{\Phi} - i\mu_{\perp} k_{\perp}^4 \rho_i^2 \times (\hat{n} + \tau \hat{\Phi}) - i \frac{\tau \nu_A^2}{c_s} \nabla_{\parallel}^{(0)} (k_{\perp}^2 \rho_i^2 \hat{\Psi}), \quad (15)$$

$$\omega \hat{n} - \omega_{*en} \hat{\Phi} = \omega_{\kappa e} (\hat{\Phi} - \hat{n}) + k_{\perp}^2 \rho_e^2 (\omega - \omega_{*en}) \hat{\Phi} - ic_s \nabla_{\parallel}^{(0)} \hat{v}_{\parallel} + i \frac{\eta_{\perp} c^2 k_{\perp}^2 c_s^2}{4\pi v_A^2} \hat{n} + i \frac{\tau v_A^2}{c_s} \nabla_{\parallel}^{(0)} (k_{\perp}^2 \rho_i^2 \hat{\Psi}), \quad (16)$$

$$(\omega + 2\omega_{\kappa i}) \hat{v}_{\parallel} + \omega_{*en} \hat{\Psi} = -ic_s \nabla_{\parallel}^{(0)} \hat{n} - 4i\mu_{\perp} k_{\perp}^2 \hat{v}_{\parallel}. \quad (17)$$

Here, $H \equiv k_{\perp}^2 \delta_e^2$, $\delta_e^2 \equiv c^2/\omega_{pe}^2$ is the electromagnetic skin depth, c is the speed of light, ω is the mode frequency, $\omega_{pe}^2 \equiv 4\pi n e^2/m_e$ is the electron plasma frequency, e is the electron charge, m_j is the mass of species j , $\mu_{\perp} \equiv 0.3\nu_{ii}\rho_i^2$ is the classical perpendicular viscosity, $\rho_i \equiv v_{ii}/\omega_{ci}$ is the ion Larmor radius, $\nu_{ii} \equiv (4/3)(\sqrt{\pi n e^4 \lambda}/\sqrt{m_i T_i^{3/2}})$, λ is the Coulomb logarithm, $v_{ii} \equiv \sqrt{T_i/m_i}$ is the ion thermal velocity, $\omega_{ci} \equiv eB/m_i c$ is the ion cyclotron frequency, m_i is the ion mass, $\tau \equiv T_e/T_i$ is the ratio of electron to ion temperature, $\rho_e \equiv v_{te}/\omega_{ce}$ is the electron Larmor radius, $v_A^2 \equiv B^2/4\pi m_i$ is the Alfvén speed, and η_{\parallel} and η_{\perp} are the longitudinal and transverse Spitzer resistivities. Here, $\hat{\Psi} \equiv e c_s \tilde{A}_{\parallel}/c T_e$, $\hat{\Phi} \equiv e \tilde{\phi}/T_e$, $\hat{v}_{\parallel} \equiv \tilde{v}_{\parallel}/c_s$, and $\hat{n} \equiv \tilde{n}/n$ are the dimensionless perturbed parallel component of vector potential, electrostatic potential, parallel ion flow, and density, respectively. The frequency ω_{*en} in Eq. (14) is the diamagnetic drift frequency [$\omega_{*en} = -(cT_e/eB)\mathbf{k} \cdot \hat{e}_{\parallel} \times \nabla \ln n$], and the frequency ω_{κ} in Eq. (15) is the curvature drift frequency ($\omega_{\kappa} \equiv \omega_{\kappa i} + \omega_{\kappa e}$) in which $\omega_{\kappa j} \equiv (2cT_j/eB)\mathbf{k} \cdot \hat{e}_{\parallel} \times \kappa$, where $\kappa = (\hat{e}_{\parallel} \cdot \nabla)\hat{e}_{\parallel}$ is the curvature vector and $c_s \equiv (T_e + T_i/m_i)^{1/2}$ is the sound speed.

III. BALLOONING EQUATIONS IN SHIFTED CIRCULAR GEOMETRY

Before considering detailed calculations of QHSs, we carry out the stability properties of a shifted circular geometry. While the geometry of this section is not a good representation for HSX plasmas, we use these calculations to compare with the stellarator specific work of the next section.

Ballooning modes are pressure-driven instabilities for modes with finite k_{\parallel} . For the interchange perturbation, the parallel component of the propagation vector is zero ($k_{\parallel}=0$), and an average minimum- B condition is stabilizing to the instability. When studying a perturbation in which $k_{\parallel} \neq 0$ but $k_{\parallel}/k_{\perp} \ll 1$, instabilities can be produced that are localized in the bad curvature region. This type of instability is called a ballooning instability. Ballooning instabilities can be resistive or ideal depending on whether the electron motion parallel to the field is impeded as a result of collisions or inductive fields. For HSX-like parameters,¹⁸ the characteristic growth rate exceeds the electron collision frequency. Therefore, the electron inertia is included in parallel Ohm's law. In this section, eigenvalue equations are derived, after employing the standard high n ballooning mode formalism,²⁴ for DRIBM, RIMHD, and IMHD modes.

The DRIBM equation can be written as follows after ignoring parallel ion momentum, perpendicular viscous stress, and the transverse particle diffusion terms and by using $\nabla_{\parallel}^{(0)} = (1/qR)d/d\theta$ in Eqs. (14)–(17):

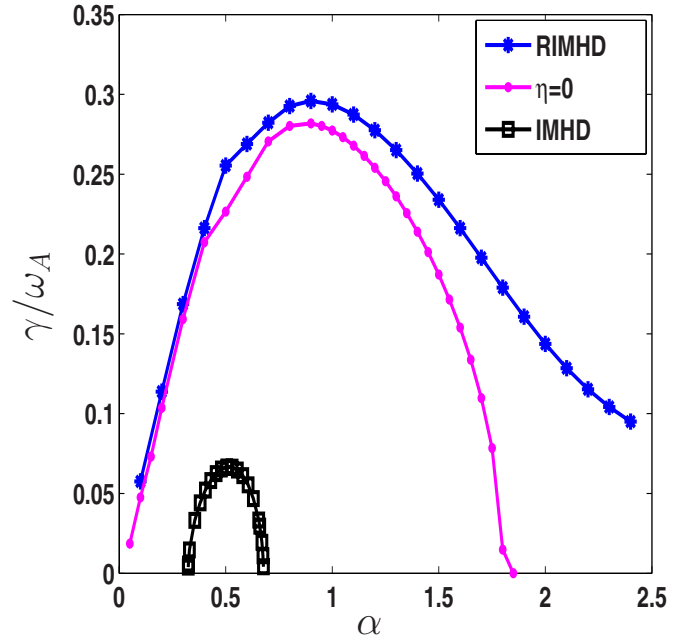


FIG. 1. (Color online) The variation of normalized growth rate is shown as a function of ballooning parameter α for $\hat{s}=0.1$, $k_{\theta}\rho_s=0.3$, $\hat{v}_e=0.023$, and $\beta=0.0002$. The squares denote IMHD stability, the large circles denote the RIMHD ballooning mode, and the smaller circles indicate the $\eta=0$ limit in the presence of nonzero electron inertia. Other than the very large α limit, the effect of resistivity on the growth rate is subdominant to the effect of the electron inertia.

$$\omega_A^2 \frac{d}{d\theta} \left(\frac{k_{\perp}^2 \rho_s^2}{\omega_{pe} + \omega_R \hat{k}_{\perp}^2} \frac{dU}{d\theta} \right) = \frac{\omega_{\kappa} (\omega_{\kappa e} - \omega_{*en}) + (\omega_{\kappa} - \omega + \omega_{\kappa i}) \omega_{pi} k_{\perp}^2 \rho_s^2}{\omega_{pe} + (1 + 1/\tau) \omega_{\kappa e} + \omega_{pi} k_{\perp}^2 \rho_s^2} U. \quad (18)$$

The quantity $U = \Phi - \hat{n}$ is the nonadiabatic response; θ is the ballooning extended poloidal variable, $-\infty < \theta < +\infty$, $\omega_A = v_A/qR$ is the Alfvén frequency where q is the safety factor and R is the major radius. $k_{\perp} = k_{\theta} \hat{k}_{\perp}(\theta)$, where $k_{\theta} = (n_{\phi} q/r)$ is the poloidal wave vector, n_{ϕ} is the toroidal mode number, and $\hat{k}_{\perp}^2(\theta) = 1 + (\hat{s}\theta - \alpha \sin \theta)^2$. $\alpha = 2q^2\beta/\epsilon_n$ is the ballooning parameter denoting the normalized pressure gradient drive and $\hat{s} = (d \ln q/d \ln r)$ is the magnetic shear. $\omega_{pj} = \omega - \omega_{*jn}$; $\rho_s \equiv c_s/\omega_{ci}$ is the ion Larmor radius, $\beta \equiv 8\pi n(T_e + T_i)/B^2$. $\omega_{\kappa e}/\omega_{*en} = \epsilon_n g(\theta)$, with $g(\theta) = [\cos \theta + (\hat{s}\theta - \alpha \sin \theta) \sin \theta]$, $\epsilon_n = L_n/R$, $L_n = (-d_r \ln n)^{-1}$; and $\omega_R = \omega \delta_e^2 k_{\theta}^2 + i\omega_{\eta}$ where $\omega_{\eta} = (c^2 \eta_{\parallel}/4\pi)(n_{\phi} q/r)^2$ is the resistive frequency.

The RIMHD incompressible ballooning equation in the high frequency ($|\omega| \gg \omega_{*en}, \omega_{\kappa e}$), long wavelength ($k_{\theta}^2 \rho_i^2 \ll 1$) limit can be written as follows:

$$\omega_A^2 \frac{d}{d\theta} \left(\frac{\hat{k}_{\perp}^2}{\omega + (\omega c^2 k_{\theta}^2/\omega_{pe}^2 + i\omega_{\eta}) \hat{k}_{\perp}^2} \frac{d\hat{\Phi}}{d\theta} \right) + \omega \hat{k}_{\perp}^2 \hat{\Phi} + \frac{\omega_{\kappa e} \omega_{*en}}{\omega k_{\theta}^2 \rho_s^2} \left(1 + \frac{1}{\tau} \right) \hat{\Phi} = 0. \quad (19)$$

Note that the electron inertia term, $\omega c^2 k_{\theta}^2/\omega_{pe}^2$, is present in Eqs. (18) and (19). The standard incompressible IMHD bal-

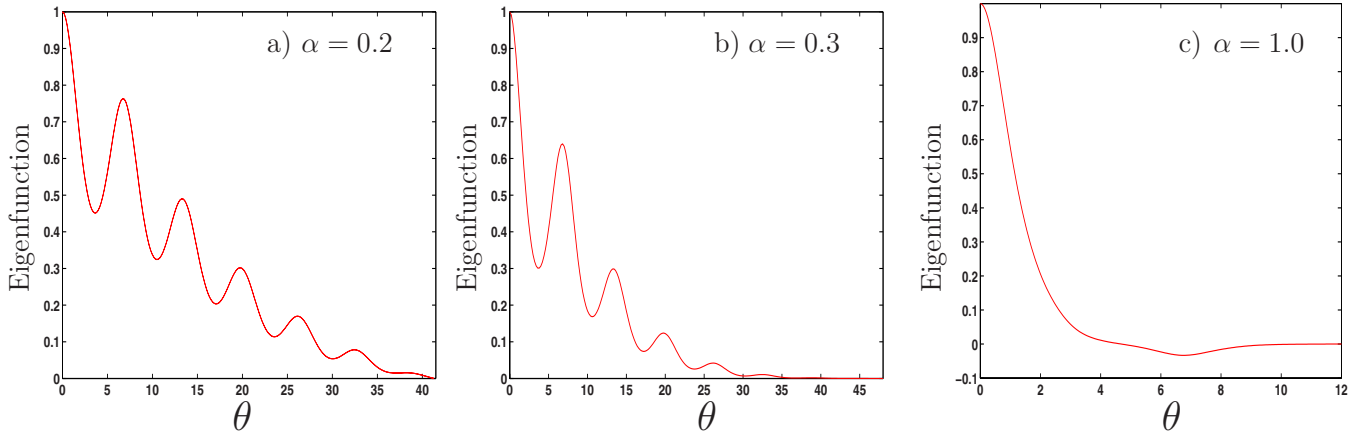


FIG. 2. (Color online) The RIMHD eigenfunction is shown as a function of θ for $\alpha=0.2$, $\alpha=0.3$, and $\alpha=1.0$.

looning equation can be recovered by neglecting electron inertia and resistivity in the RIMHD equation, Eq. (19),

$$\omega_A^2 \frac{d}{d\theta} \left(\hat{k}_\perp^2 \frac{d\phi}{d\theta} \right) + \omega^2 \hat{k}_\perp^2 \phi + \frac{\omega_{ke} \omega_{*in}}{k_\theta^2 \rho_i^2} \left(1 + \frac{1}{\tau} \right) \phi = 0, \quad (20)$$

where the usual FLR effect (for $k_\perp \rho_i \ll 1$) can be included by substituting $\omega(\omega - \omega_{*in})$ for ω^2 in Eq. (20).

A. Results in shifted-circular geometry

The differential Eqs. (18)–(20) are solved by the Runge–Kutta fourth order integrator and Muller’s method of root finding is used. The complex eigenvalue is iterated until the following boundary condition is satisfied:

$$\frac{d\phi(\theta=0)}{d\theta} = 0, \quad \phi(\theta \rightarrow \infty) \rightarrow 0. \quad (21)$$

Equations (18)–(20) are solved numerically for axisymmetric shifted-circle equilibria, which are the equilibria used in obtaining the results shown in Figs. 1–6. For all cases, the parameters used are those appropriate for HSX edge plasmas ($r/\bar{a} \sim > 0.7$): $T_e = 100$ eV, $T_i = 25$ eV, $B \approx 0.5$ T, $n_e \approx 10^{18}$ m $^{-3}$, $q = 1.0$, $\hat{s} = -0.03$, and $\beta = 2 \times 10^{-4}$.¹⁹

Figure 1 shows the normalized growth rate (γ/ω_A) of the IMHD, RIMHD, and IMHD modes with electron inertia (RIMHD in the limit of $\eta=0$) as a function of the normalized pressure gradient (the ballooning parameter α), for $\theta_k=0$, $\hat{s}=0.1$, $k_\theta \rho_s = 0.3$, $\hat{v} = v_{ei}/\omega_A = 0.023$, and $\beta = 0.0002$. In this scan, a positive global magnetic shear, $\hat{s} = 0.1$, is chosen to illustrate the IMHD unstable region. HSX has reverse shear in the tokamak sense (negative value of \hat{s}). However, the magnetic geometry of the shifted circle is completely inappropriate to model HSX plasmas. In the presence of 3D shaping, IMHD ballooning instabilities can be excited when $\hat{s} < 0$.²⁵

The electron inertia and resistivity result in an instability when the IMHD mode is stable. The electron inertia and resistive modes are purely growing ($\omega_r = 0$). For HSX-relevant parameters, the electron inertia modes (the RIMHD case for $\eta=0$) are found to be more important than the resistive modes due to the existence of RIMHD modes in the first ideal stability region. Note that RIMHD modes persist in

the IMHD second stable regime. Both the electron inertia and resistive instabilities are characterized by broad eigenfunctions along the field lines as shown in Figs. 2(a) and 2(b). The eigenfunctions are found to be relatively strongly localized along the field line at higher values of the ballooning parameter α , as shown in Fig. 2(c). Moreover, the qualitative nature of the eigenfunctions is insensitive as to whether or not electron inertia is present. The electron inertia and resistive ballooning eigenfunctions are found to be broad for HSX-relevant values of the ballooning parameter ($\alpha \ll 1$). The broad eigenfunction in extended poloidal angle θ describes that the mode is weakly ballooning. Therefore, the assumptions $|\omega| \gg \omega_{*en} \gg \omega_{ke}$ and $k_\theta^2 \rho_i^2 \ll 1$ needed for MHD applicability become suspect and, for a more satisfactory stability analysis, a two fluid formulation is required.

Figure 3 shows the eigenvalues obtained for the DRIBM derived using Eq. (18) in which diamagnetic and first order FLR effects are included. The growth rates of DRIBM are compared with the growth rates of RIMHD modes using the same parameter values as used in Fig. 1, except choosing stellaratorlike global shear $\hat{s} = -0.03$ and $k_\theta \rho_s = 0.1$. The FLR and diamagnetic effects are found to be slightly stabilizing for RIMHD modes that propagate in the electron diamagnetic flow direction. These stabilizing effects increase the critical α in the first stability region. The RIMHD modes are

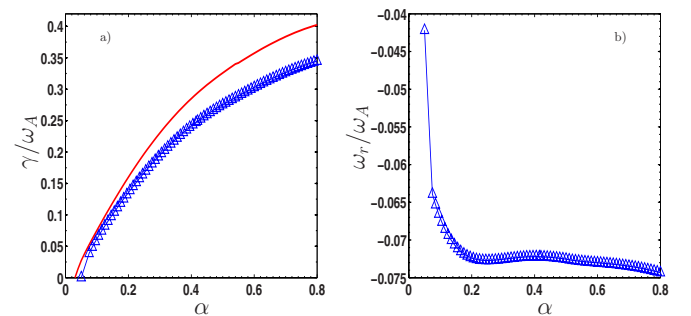


FIG. 3. (Color online) (a) Growth rate and real part of the frequency (b) of the ballooning mode as a function of α for the RIMHD model (solid line) and the model with drift effects (DRIBM with Δ symbols) for $\hat{s} = -0.03$ and $k_\theta \rho_s = 0.1$. The other parameters are the same as those used in Fig. 1. The real frequency is in the ion diamagnetic direction.

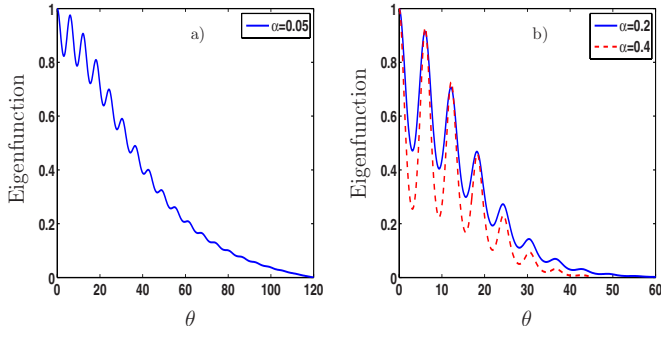


FIG. 4. (Color online) (a) The eigenfunction of the DRIBM as a function of θ for $\alpha=0.05$, and (b) $\alpha=0.2$ and $\alpha=0.4$.

purely growing (zero real frequency). The real frequency of the DRIBM mode is shown in Fig. 3(b) where negative values of ω_r indicate mode frequencies in the ion diamagnetic direction. All of these modes are still characterized by broad eigenfunctions in ballooning space. This indicates a strong radial localization in configuration space. As shown in Fig. 4(b), the width in ballooning space decreases as the ballooning parameter α increases.

In Fig. 5, the variation of the normalized growth rate and real frequency for the DRIBM are shown as a function of global magnetic shear \hat{s} with $\alpha=0.1$. The other parameters are the same as in Fig. 3. A reversed magnetic shear is found to be more stabilizing than positive magnetic shear because the normal and geodesic curvature in the function $g(\theta)=[\cos \theta+(\hat{s}\theta-\alpha \sin \theta)\sin \theta]$ counteract each other and reduce the destabilizing toroidal effects.⁴ We reiterate that the geometry of the shifted circle is inappropriate for direct HSX comparison. Nonetheless, some inferences from these calculations can be made. The effects of reversed magnetic shear not only reduce the growth rate but, also, extend the eigenfunction along the ballooning angle, as shown in Fig. 6. HSX presents a nearly flat q -profile, a low local magnetic shear and an unfavorable magnetic curvature at the $\theta=0=\zeta$ point of the magnetic surface, where θ and ζ are the extended poloidal and toroidal angle like coordinates (see for detail in Sec. III B). Therefore, DRIBM modes will be unstable in a device with the HSX geometry because these types of modes have large amplitude (balloon) in the region of bad local curvature (for the instability drive) and low local magnetic field shear (to minimize stabilizing effect of field line bend-

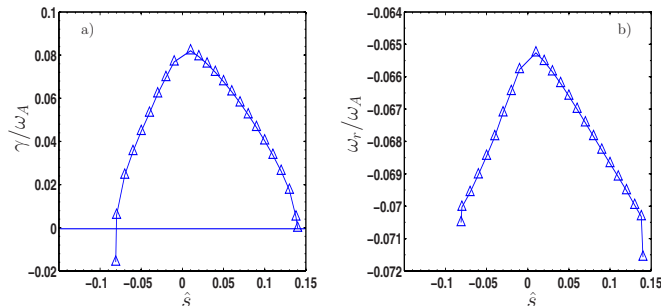


FIG. 5. (Color online) (a) Growth rate and real frequency (b) for the DRIBM mode as a function of \hat{s} for $q=1.0$, $k_{\theta}\rho_s=0.1$, $\alpha=0.10$, $\tau=1.0$, $\beta=0.002$, and $\epsilon_n=0.07$.

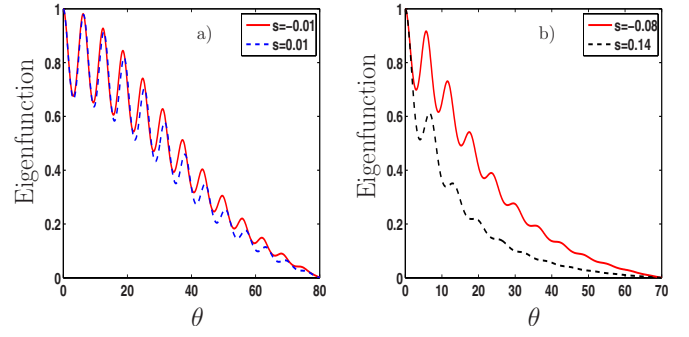


FIG. 6. (Color online) The DRIBM eigenfunction as a function of θ for positive and negative values of shear.

ing) within each field period. The unstable modes have an envelope that extends over many field periods along field lines. Hence, the modes are highly localized radially.

The growth rate is plotted in Fig. 7(a) as a function of $k_{\theta}\rho_s$ with $\hat{s}=-0.03$ for the RIMHD and DRIBM instabilities. The other parameters are the same as used to obtain the results shown in Fig. 3. All parts of the k -spectrum are found to be unstable in the incompressible RIMHD mode. However, for the DRIBM instability, the diamagnetic and FLR effects reduce the growth rate and completely stabilize the mode for $k_{\theta}\rho_s \geq 0.2$. Even for $k_{\theta}\rho_s \rightarrow 0$, the growth rate of the DRIBM instability is found to be smaller than the growth rate of the RIMHD instability, which indicates the stabilizing effects of the secularity of the magnetic drift frequency. The real frequency of the DRIBM mode is shown in Fig. 7(b) is found to decrease with increasing $k_{\theta}\rho_s$. Generally, two fluid effects are found to be stabilizing for the RIMHD mode. Note that the ion temperature gradient, the parallel ion dynamics, and $\mathbf{E} \times \mathbf{B}$ flow shear are not included in these numerical results. These effects can all decrease the growth rate of the DRIBM further. For the chosen plasma parameter values, the inclusion of temperature gradient can lead to FLR stabilization for values of $k_{\theta}\rho_s$ smaller than 0.2. However, for flow shear stabilization, one would apparently need $\gamma < \omega_E \approx 30E_r$, or $E_r > 100$ V/cm. Additionally, since $T_i \ll T_e$ in HSX plasmas, one would not expect ion temperature gradient effects to play an important role.

The dependence of γ and ω on the density scale length $\epsilon_n=L_n/R$ where $L_n=(d_r \ln n)^{-1}$ is shown in Figs. 8(a) and 8(b) for $q=1.0$, $\hat{s}=-0.03$, $\alpha=2q^2\beta/\epsilon_n$, $\tau=1.0$, $\beta=0.002$,

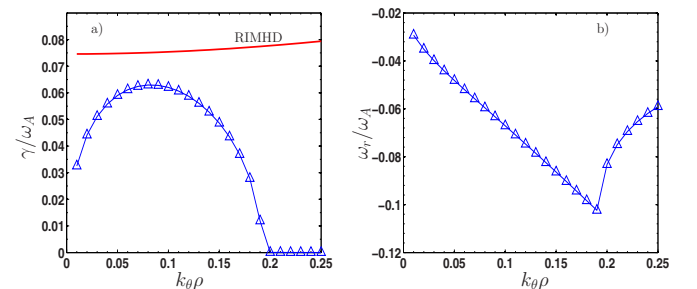


FIG. 7. (Color online) (a) Growth rate and real frequency (b) for RIMHD modes (solid line) and the DRIBM (Δ symbols) modes, and as a function of $k_{\theta}\rho$ for $\hat{s}=-0.03$. The other parameters are the same as those used in Fig. 3.

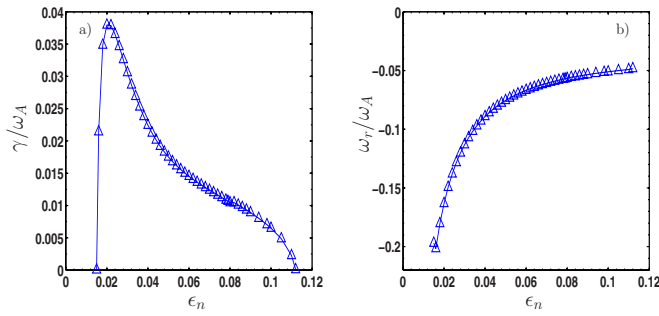


FIG. 8. (Color online) (a) Growth rate and real frequency (b) for the DRIBM as a function of ϵ_n for $k_{\theta}\rho_s=0.1$, $\alpha=2q^2\beta/\epsilon_n$. The other parameters are the same as those used in Fig. 3.

$k_{\theta}\rho_s=0.1$, and $\theta_k=0$. It is found that as ϵ_n increases, the growth rate decreases, while the real frequency also decreases in magnitude. The mode is completely stabilized for $\epsilon_n \leq 0.02$ and for $\epsilon_n \geq 0.112$. For small ϵ_n , the mode is stable since $|\omega_{\kappa}|/\omega \ll 1$ and for $\epsilon_n \geq 0.112$, the mode vanishes due to compressibility effects. At low density gradients, growth rates decrease and the eigenfunction becomes broader along the field line as shown in Fig. 9.

The variation of the growth rate and real frequency is shown in Fig. 10 as a function of β for $k_{\theta}\rho_s=0.01$, and $\tau=0.025$, where the other parameters are the same as those used to obtain the results shown in Fig. 8. In this small $k_{\theta}\rho_s$ limit, there is no instability threshold at low values of β . However, as β increases above 0.05, the growth rate and real frequency decrease and the mode becomes completely stabilized at $\beta=0.17$. This is due to ω_* stabilization at high β . As shown in Fig. 11, the resistive and inertia effects become unimportant for $\beta \sim 0.17$, and the transition to an ideal mode results under these conditions.

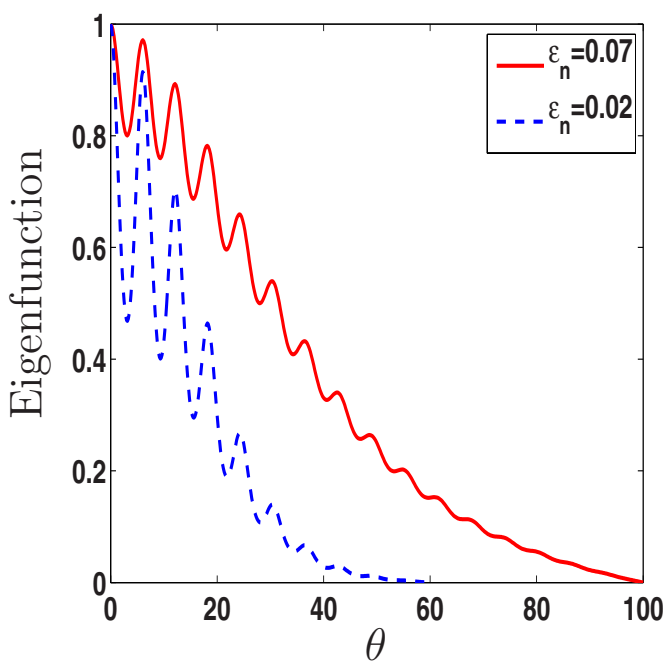


FIG. 9. (Color online) The DRIBM eigenfunction is plotted for $\epsilon_n=0.02$ and $\epsilon_n=0.07$.

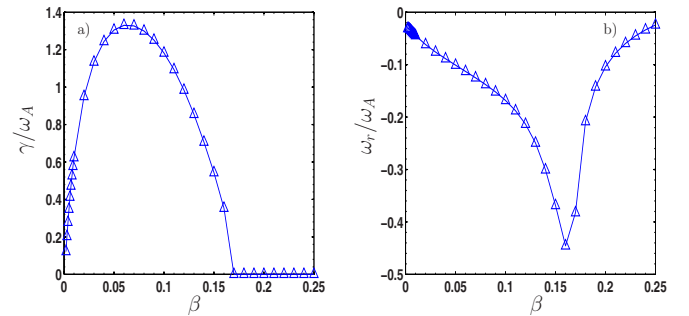


FIG. 10. (Color online) (a) Growth rate and real frequency (b) for the DRIBM as a function of β for $\epsilon_n=0.07$, $\alpha=2q^2\beta/\epsilon_n$, $q=1.0$, $k_{\theta}\rho_s=0.01$, and $\tau=0.25$.

In order to illustrate the DRIBM mode threshold as a function of β , the growth rate and real frequency are plotted in Figs. 12(a) and 12(b) as a function of β for $k_{\theta}\rho_s=0.2$ and $\tau=4.0$, where the other parameters are the same as employed in Fig. 10. Note that unlike the results from Figs. 10 and 11, the calculations for Figs. 12 and 13 have a much larger k_{θ} (and hence more prominent drift physics) and higher electron temperature. For $k_{\theta}\rho_s=0.2$, and for higher electron temperature plasmas, the stability threshold is found at $\beta \approx 0.006$. The ballooning mode eigenfunction is shown in Fig. 13 as a function θ for $\beta=0.006$ and $\beta=0.012$.

B. Results for a plasma with HSX geometry

The four-field period HSX is a QHS experiment at the University of Wisconsin-Madison.¹⁸ HSX has a major radius of 1.2 m and a minor radius of 0.09–0.13 m, depending on the machine configuration. It is a unique toroidal experiment that has an aspect ratio of eight, but an average toroidal curvature close to zero. It has a helical axis of symmetry that

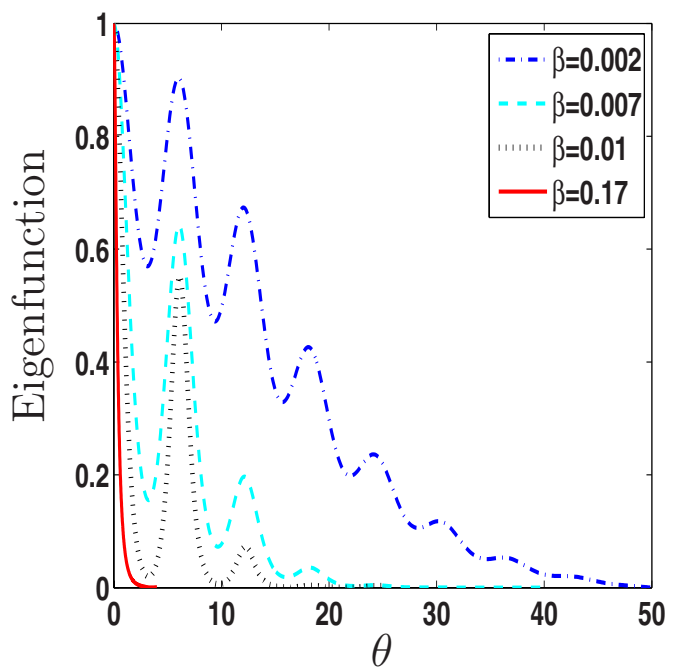


FIG. 11. (Color online) The DRIBM eigenfunction is plotted as a function of θ for four values of β .

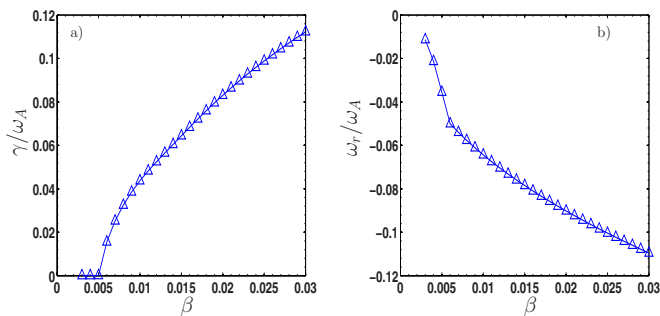


FIG. 12. (Color online) (a) Growth rate and real frequency (b) for the DRIBM as a function of β for $k_{\perp}\rho_s=0.2$ and $\tau=4.0$. The other parameters are the same as those used in Fig. 10.

is similar to the helical symmetry present in a straight stellarator. By restoring a direction of symmetry to a toroidal stellarator, the quasihelical stellarator solves one of the fundamental disadvantages of conventional stellarators, which has higher neoclassical transport. In addition to the modular coils that provide the base QHS configuration, there is an additional set of auxiliary coils that break the helical symmetry and allow the neoclassical transport and the stability limit to be independently controlled. Specifically, operating HSX in the mirror mode configuration (a configuration in which the quasisymmetry is broken with the addition of a toroidal mirror term to the magnetic spectrum)¹⁸ increases the neoclassical transport and parallel viscous damping by orders of magnitude (back to the level of conventional stellarators) without appreciable changes in the rotational transform, magnetic well depth, or ideal local MHD stability limit. Neoclassical transport is optimized in QHS, and it is likely that DRBMs play an important role in producing edge plasma fluctuations and anomalous transport in the QHS. In

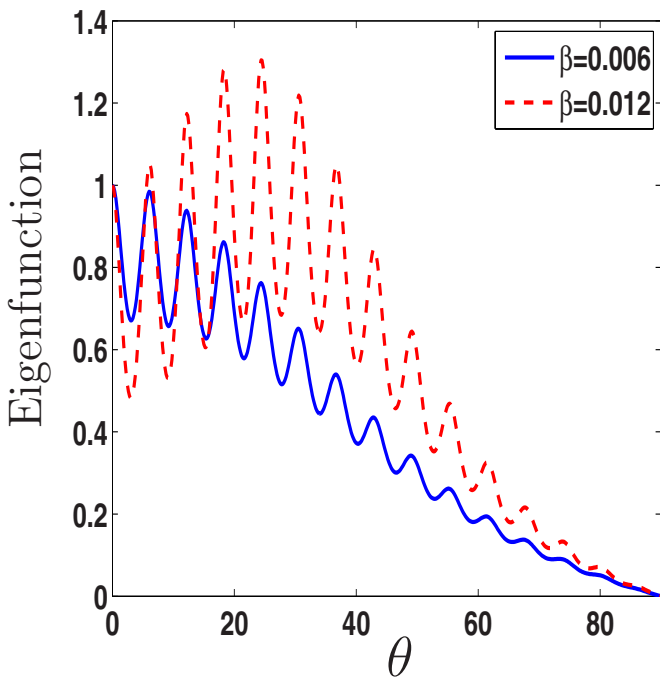


FIG. 13. (Color online) The DRIBM eigenfunction is plotted as a function of θ for $\beta=0.006$ and $\beta=0.012$.

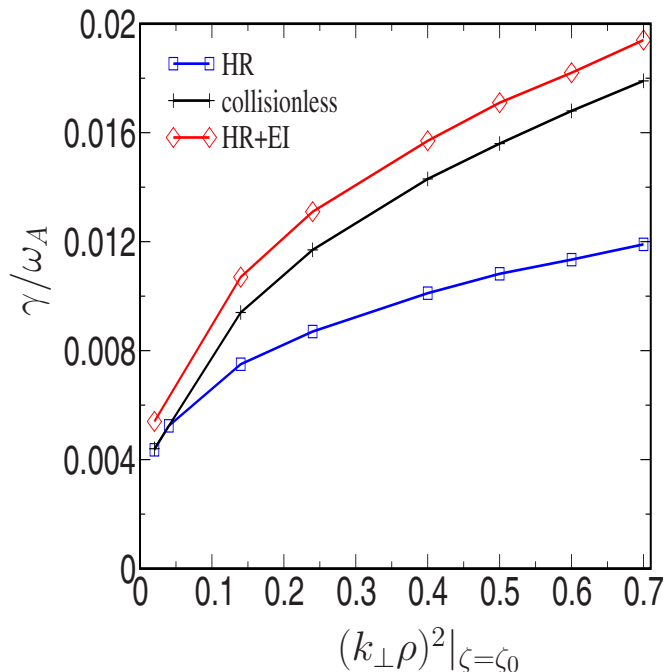


FIG. 14. (Color online) Growth rate for the RIMHD ballooning modes in the electrostatic limit as a function of $(k_{\perp}\rho)^2$ in QHS configuration for $s=0.8980$, $\tau=1$, $Rv_{ei}/2c_s=0.42$, $\theta_k=0.0$, $\epsilon_n=0.07$, and $\theta_0=0$, $\zeta_0=0$ field line.

this section DRBMs are studied in the QHS configuration and the results are compared and contrasted with the results of a mirror configuration, which has high neoclassical transport.

Equation (19) is solved numerically in the electrostatic limit using a fully three-dimensional MHD equilibria for a QHS stellarator and a configuration whose symmetry is spoiled by the presence of magnetic mirror contribution to the magnetic spectrum. The ballooning mode formalism and WKB type boundary conditions^{26,27} are used to solve an eigenvalue problem for the RIMHD equation in the electrostatic limit using a fully three-dimensional hydrodynamic equilibria. The equilibria are computed using the VMEC code²⁸ with fixed boundary conditions for QHS and mirror mode configurations and for a set of 98 magnetic surfaces. The VMEC coordinate system is not a straight field line coordinate system. Thus, before the RIMHD ballooning equation is solved in the electrostatic limit, the equilibria are first transformed²⁹ to Boozer flux coordinates (s, θ, ζ) .³⁰ Then, the contravariant and covariant basis vectors are constructed for each flux surface and used to calculate the magnetic field, the magnetic field line curvature, the local magnetic shear, and the derivatives of the magnetic field in a fully three dimensional configuration. The coordinate $s=2\pi\psi/\psi_p$ is the normalized flux (radial) coordinate.³¹ By construction, the radial label ranges from 0 (at the magnetic axis) to 1 (at the last closed magnetic surface). Here $2\pi\psi$ is the poloidal magnetic flux bounded by the magnetic axis and the $\psi=\text{const.}$ surface and $\psi_p=\pi B_o \bar{a}^2/q$, the total poloidal magnetic flux. Here B_o is the magnetic field at the axis, \bar{a} is the average minor radius, $q=2\pi/\iota$ is the safety factor, and $\iota=\iota(\psi)$ is the rotational transform. The θ and ζ are generalized poloidal and toroidal

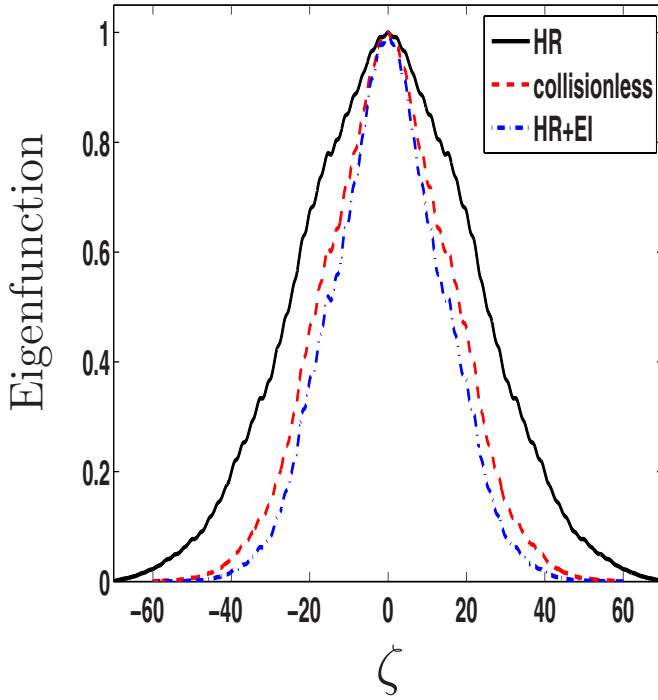


FIG. 15. (Color online) The RIMHD eigenfunctions as a function of θ for $(k_{\perp}\rho)^2=0.24$. The other parameters are the same as those used in Fig. 14.

angles. A given magnetic flux surface can be represented by a square cell $0 \leq \theta < 2\pi$, $0 \leq \zeta < 2\pi$ with the edges $\theta=0, 2\pi$ and $\zeta=0, 2\pi$ topologically identified. The equilibrium is periodic in ζ and θ for the eigenvalue problem along the field line. However, the magnetic field lines lie in the domain $-\infty < \theta < \infty$, $-\infty < \zeta < \infty$, which is usually referred to as a covering space.³² The details of magnetic field configuration are described in Ref. 33.

The drift wave Eq. (19) is solved by a shooting algorithm using a sixth-order Numerov scheme and WKB type boundary conditions and by demanding continuity of the function at its first derivative at a matching point. Details of the boundary conditions and the numerical method used are given in Ref. 27.

Figure 14 contains a plot of the growth rate γ , normalized by ω_A , as a function of $(k_{\perp}\rho)^2$ (evaluated at $\zeta=\zeta_0$) for $\tau=1$, $R\nu_{ei}/2c_s=0.42$, $\epsilon_n=0.07$, and $\theta_k=0.0$ (where θ_k is the radial mode number). These parameters used are those correspond to the HSX edge plasmas. This calculation is carried out for the field line that intersects the location $\theta_0=0$, $\zeta_0=0$ on the normalized magnetic surface $s=0.8980$ as given in Refs. 31 and 33. This point is chosen because it is thought to be the most unstable since the local magnetic shear is small, the local value of the geodesic curvature is zero, and the destabilizing influence of the normal curvature is strongest. In Fig. 14, the bottom curve, denoted with squares, is for the highly resistive case (HR), where $\delta_e=0$, $\nu_e \neq 0$; the middle curve, denoted by x, is for the collisionless case ($\nu_e=0$, $\delta_e \neq 0$). The top curve, denoted by diamonds, is for nonzero electron inertia and collisionality (EI+collisions). All three cases are found to be unstable for QHS relevant parameters, and, in each case, the growth rate increases with increasing mode number. The corresponding mode structures

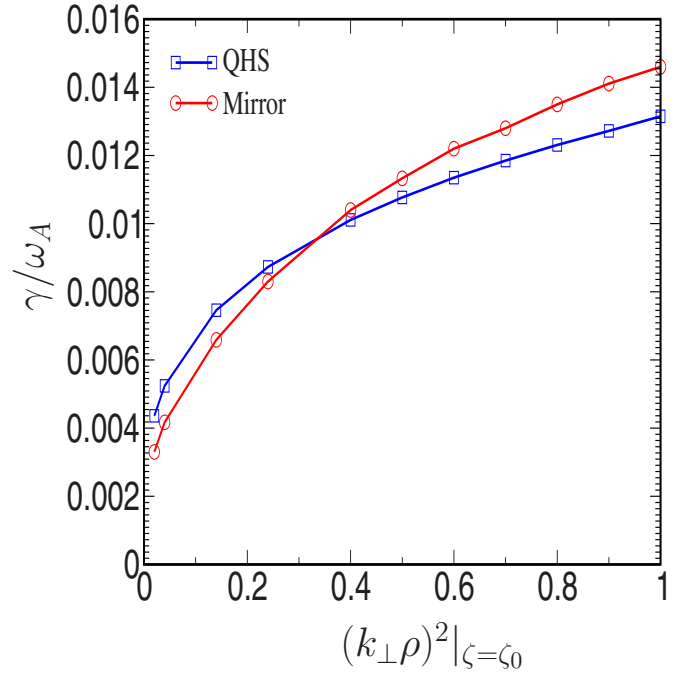


FIG. 16. (Color online) Growth rate for the RIMHD ballooning modes in the electrostatic limit as a function of $(k_{\perp}\rho)^2$ for QHS and mirror cases. The other parameters are the same as those used in the Fig. 14.

are shown in Fig. 15 for $(k_{\perp}\rho)^2=0.24$. In comparison with the ion temperature gradient and drift modes calculated in the electrostatic limit in earlier publications,^{21,33} these modes are found to be very extended ($\zeta_0=20\pi$) along the magnetic field line. However, as the growth rate increases for each of the cases, the eigenfunctions become relatively localized.

The highly resistive (HR: $\delta_e=0$, $\nu_e \neq 0$) growth rate in QHS, compared to the growth rate for the corresponding mirror case is illustrated in Fig. 16. In both configurations, the magnitudes of the linear growth rates are found to be comparable, indicating roughly the same level of anomalous transport flux that is observed in the edge region of experiments.³⁴ This result is consistent with our earlier findings for ITG and drift modes.^{21,33} The common stability properties are due to the similar structure of the curvature and the local magnetic shear. The corresponding ballooning mode eigenfunctions are shown in Figs. 17(a) and 17(b) as a function ζ for $(k_{\perp}\rho)^2=0.02$ and $(k_{\perp}\rho)^2=0.6$.

The shifted circular geometry is very different in the QHS and mirror geometries. However, the magnitude of the growth rates in all three geometries is found to be comparable and the eigenfunctions, in all cases, are extended along the magnetic field lines and have similar structure. The periodicity in the eigenfunctions is different in the shifted circular geometry relative to the HSX geometries.

IV. THE PARTICLE DIFFUSIVITY IN THE STRONG BALLOONING LIMIT

HSX is a low magnetic shear stellarator. In a plasma with low shear, the RBM modes are expected to be extended along the magnetic field lines. This is shown in Secs. III A and III B by computing eigenfunctions of RBMs in various

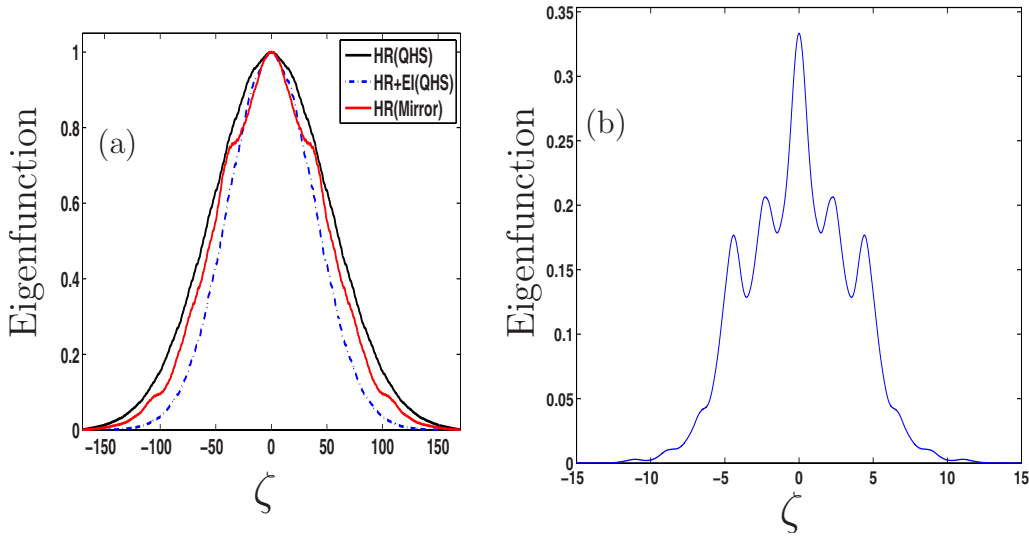


FIG. 17. (Color online) (a) The RIMHD eigenfunctions as a function of ζ for $(k_{\perp}\rho)^2=0.02$ and (b) $(k_{\perp}\rho)^2=0.6$. The other parameters are the same as those used in the Fig. 14.

limits as a function of ballooning angle θ . In the previous sections, second order differential eigenvalue equations are solved numerically in different limits by using a standard shooting technique. In this section the full RBM model [Eqs. (14)–(17)] is solved to estimate the effective particle diffusivity (D_n) in a strong ballooning limit. The algebraic method is used to calculate eigenvalues and eigenvectors. The effective particle diffusivity is computed directly from the eigenvalues and the eigenvectors.

The flux of particles produced by the perturbed $\mathbf{E} \times \mathbf{B}$ motion of the plasma is

$$\Gamma = \tilde{n}\tilde{v}_E^* + \text{c.c.} = 2(\text{Re } \tilde{n} \text{ Im } \tilde{\phi} - \text{Im } \tilde{n} \text{ Re } \tilde{\phi})k_y/B. \quad (22)$$

The saturation level of the turbulence is computed using the quasilinear approximation

$$\frac{e\tilde{\phi}}{T_e} \approx \frac{1}{k_x\rho_s} \frac{\gamma}{k_y c_s} = \frac{2}{Rk_x} \frac{\gamma}{\omega_{\kappa e}}, \quad (23)$$

which is used to compute the particle flux given by

$$\frac{\Gamma Rk_x^2}{n \omega_{\kappa e}} = 2\hat{\gamma}^2(\text{Re } \hat{n} \text{ Im } \hat{\Phi} - \text{Im } \hat{n} \text{ Re } \hat{\Phi})/|\hat{\Phi}|^2, \quad (24)$$

where $\hat{\gamma} = \gamma/\omega_{\kappa e}$ is the growth rate normalized to the electron magnetic drift frequency.

In order to estimate particle diffusivity due to DRIBM in the HSX stellarator the following values are considered: $n=10^{18} \text{ m}^{-3}$, $\mu_{\perp}=0.0$, $B=0.5 \text{ T}$, $\bar{a}=0.12 \text{ m}$, $\bar{R}=1.2 \text{ m}$, $q=1.0$, $\hat{s}=0.03$, $Z_{\text{eff}}=1.5$, $\nabla T_i=0.0$, and $k_{\perp}\rho_s=0.1$. The value of $k_{\perp}\rho_s=0.1$ is chosen because at this wavelength the growth rate is found (using the shooting method, see Fig. 4) to be maximum for the DIRBM mode. The expression for parallel wavenumber $k_{\parallel} = \sqrt{\alpha}/(qR)$ is used, which is estimated in Ref. 35 in terms of the ballooning parameter α by

$$\alpha = (k_1 + \sqrt{k_1 + \hat{s}^2 k_2})/2, \quad (25)$$

with

$$k_1 = \frac{q^2}{4}(k_{\perp}\rho)^2 \sqrt{\frac{T_i}{T_e} \frac{(g_{Ti} + g_n)}{2(1-f_t)}}, \quad (26)$$

$$k_2 = q^2(k_{\perp}\rho)^4 \frac{T_i}{T_e} \frac{(g_{Ti} + g_n)}{2(1-f_t)}, \quad f_t \approx \sqrt{\frac{2\epsilon_H}{1 + \epsilon_H}},$$

where f_t is the trapped electron fraction, $\epsilon_H=1.4 r/E$ is the helical ripple in HSX, g_{Ti} and g_n are the normalized ion temperature and density gradients [$g_{ji} \equiv 1/\epsilon_j$, $\epsilon_j=L_j/R$, $L_j=(-d_r \ln j)^{-1}$].

Figure 18 shows the effective particle diffusivity D_n due to a full DRIBM model (the solid curve) plotted against the normalized density gradient, $1/\epsilon_n$. The effect of omitting electron inertia, indicated by the curve denoted with squares, and the effect of omitting parallel ion dynamics, indicated by the dashed curve, are also illustrated. It is seen that D_n increases with density gradients. The magnitude of the particle diffusivity is in the range (5–10 m^2/s), which is comparable to the experimental measured particle diffusivity at the edge of HSX plasmas.¹⁹ The stabilizing effects of parallel ion dynamics ($v_{\parallel} \neq 0$) are found to be very small due to the small ion temperature. Electron inertia effects are found to have an effect only for large density gradients. Note that these results are presented in the limit of strong ballooning, where electron inertia is not expected to play a dominant role due to a strong localization of the eigenfunctions.

Figure 19 shows the effective particle diffusivity plotted against the normalized density gradient $1/\epsilon_n$, for electron temperature T_e as a parameter. In this scan electron temperatures $T_e=10, 20, 30,$ and 40 eV are considered while the ion temperature $T_i=10 \text{ eV}$ is assumed. The selected values of electron and ion temperatures are appropriate for the edge region of HSX plasmas. It is observed that the particle diffusivity D_n increases with decreasing electron temperature.

The particle diffusivity D_n dependence on electron ion collision frequency (ν_{ei}) is shown in Fig. 20 with

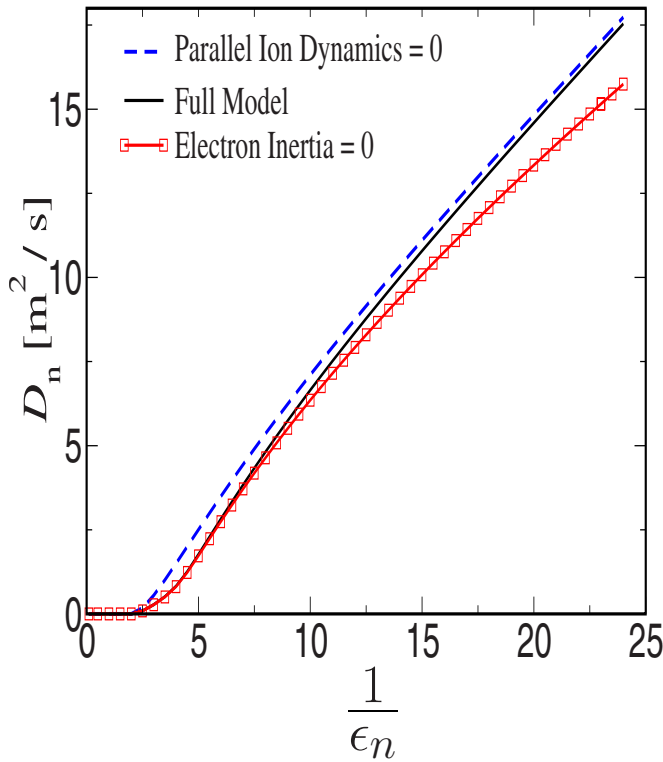


FIG. 18. (Color online) The effective particle diffusivity D_n plotted against the normalized density gradient, $1/\epsilon_n$ for full model (the solid curve), ignoring electron inertia from the full model (the curve denoted with dashes) and ignoring the parallel ion dynamics (the dashed curve) from the full model for $n=10^{18} \text{ m}^{-3}$, $\mu_{\perp}=0.0$, $B=0.5 \text{ T}$, $\bar{a}=0.12 \text{ m}$, $\bar{R}=1.2 \text{ m}$, $q=1.0$, $\hat{s}=0.03$, $Z_{\text{eff}}=1.5$, $\nabla T_i=g_{T_i}=0.0$, and $k_{\perp}\rho_s=0.1$.

$1/\epsilon_n=10.0$ and $\tau=T_e/T_i=2.0$. All other HSX parameters are the same as those used in Fig. 18. It is found that as electron collision frequency increases, the particle transport increases as well. In summary, the increase at low electron temperature seen in particle diffusivity with density gradient and collisionality indicates that the DRIBM model predicts an increase in transport with radius as observed in edge region of the HSX stellarator.¹⁹

Certainly there is critical density gradient over which drift RBM becomes unstable. In the plasma core region where the temperature is large this mode does not contribute to transport. However the mode can provide substantial transport in the edge region due to steep density gradient and small temperature. In order to give a value for critical gradient and its dependence on plasma and device parameters required a large number of scans which is beyond the scope of current paper.

V. CONCLUSIONS

A unified theory that includes both resistive and electron inertial ballooning modes has been developed. The DRIBM is characterized by eigenfunctions that are extended along the field line in ballooning space. The qualitative nature of the eigenfunctions is found to be insensitive to whether or not electron inertia is present. However, the resistive and inertial effects become unimportant as the plasma β is increased close to the transition to an IMHD mode. In the

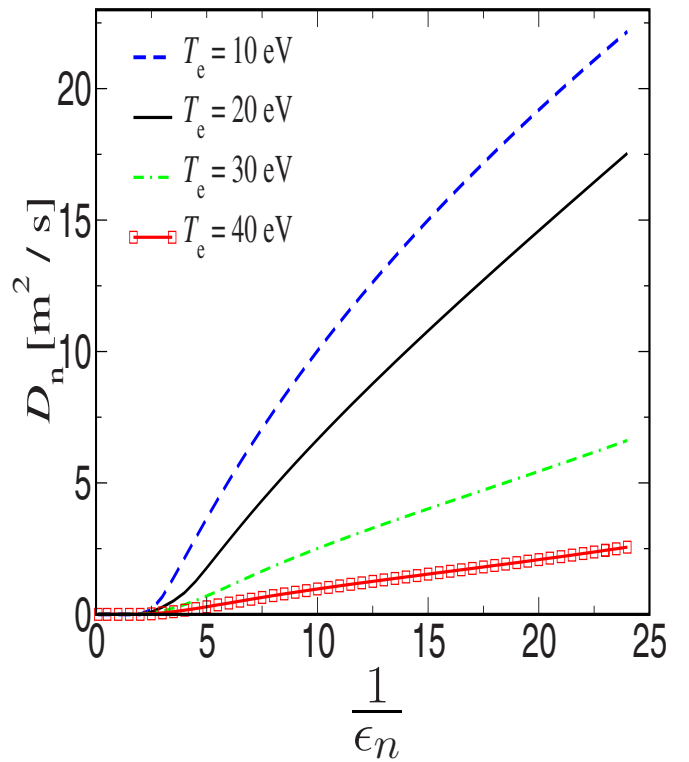


FIG. 19. (Color online) The effective particle diffusivity D_n plotted against the normalized density gradient, $1/\epsilon_n$ for full model for $T_e=10, 20, 30, 40$, and $T_i=10 \text{ eV}$. The other parameters are the same as those used in Fig. 18.

absence of two fluids drifts effects, the modes are purely growing and they persist in regimes where IMHD ballooning modes are stable. For parameters of interest to HSX, electron inertia effects are more important than plasma resistivity. The magnitude of the linear growth rates is not sensitive to the

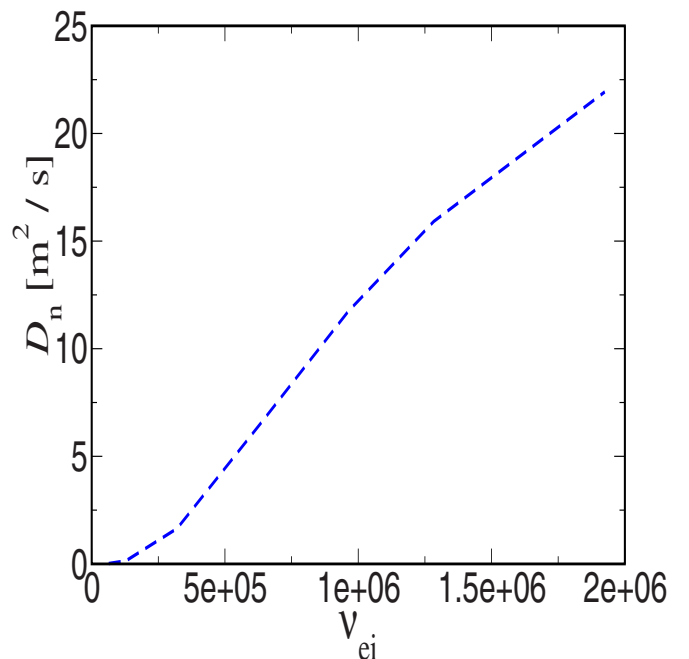


FIG. 20. (Color online) The effective particle diffusivity D_n plotted against the electron ion collision frequency, ν_{ei} , for full model for $T_e=20 \text{ eV}$, and $T_i=10 \text{ eV}$. The other parameters are the same as those used in Fig. 18.

magnetic configuration in HSX plasmas. This result would indicate a comparable level of anomalous transport in QHS and mirror configurations and is consistent with experimental observations in the edge region of the HSX stellarator.³⁴ The common stability properties in the QHS and mirror configurations in the HSX are due to the similar structure of the curvature and local magnetic shear. The observation of critical density gradient shows that the DRBMs do not contribute to transport in the central core region as a consequence of the large electron temperature. The increase in particle diffusivity with increasing density gradient and collisionality at low electron temperature indicates that the DRIBM may be responsible for the increase in transport with radius observed in HSX plasma edge region. Moreover, the magnitude of the particle diffusivity is estimated to be in the range of experimentally measured particle diffusivity at the edge of the HSX stellarator plasma.¹⁹

ACKNOWLEDGMENTS

This research was supported by the U.S. DOE under Grant Nos. DE-FG02-99E54546, DE-FG02-86ER53218, and DE-FG02-92ER54141.

- ¹G. Bateman and D. Nelson, *Phys. Rev. Lett.* **41**, 1804 (1978).
- ²B. A. Carreras, P. H. Diamond, M. Murakami, J. L. Dunlap, J. D. Bell, H. R. Hicks, J. A. Holmes, C. E. Thomas, and R. M. Weiland, *Phys. Rev. Lett.* **50**, 503 (1983) (and references therein).
- ³J. R. Myra, D. A. D'Ippolito, X. Q. Xu, and R. H. Cohen, *Phys. Plasmas* **7**, 4622 (2000).
- ⁴J. Weiland, *Collective Modes in Inhomogeneous Plasma* (IOP, Bristol, 2000).
- ⁵A. Zeiler, J. F. Drake, and B. Rogers, *Phys. Plasmas* **4**, 2134 (1997).
- ⁶R. G. Kleva and P. N. Guzdar, *Phys. Plasmas* **6**, 116 (1999).
- ⁷J. W. Connor and R. J. Hastie, *Phys. Plasmas* **6**, 4260 (1999).
- ⁸R. H. Hastie, J. J. Ramos, and F. Porcelli, *Phys. Plasmas* **10**, 4405 (2003).
- ⁹P. N. Guzdar, J. F. Drake, D. McCarthy, A. B. Hassam, and C. S. Liu, *Phys. Fluids B* **5**, 3712 (1993).
- ¹⁰B. N. Rogers and J. F. Drake, *Phys. Plasmas* **6**, 2797 (1999).
- ¹¹X. Q. Xu, R. H. Cohen, T. D. Rognlien, and J. R. Myra, *Phys. Plasmas* **7**, 1951 (2000).
- ¹²A. H. Glasser, J. M. Greene, and J. L. Johnson, *Phys. Fluids* **18**, 875 (1975).
- ¹³X. Llobet, H. L. Berk, and M. N. Rosenbluth, *Phys. Fluids* **30**, 2750 (1987).
- ¹⁴D. Correa-Restrepo, *Z. Naturforsch. A* **37**, 848 (1982).
- ¹⁵H. R. Strauss, L. E. Sugiyama, G. Y. Fu, W. Park, and J. Breslau, *Nucl. Fusion* **44**, 1008 (2004).
- ¹⁶R. Kaiser, *Nucl. Fusion* **33**, 1281 (1993).
- ¹⁷T. Rafiq, C. C. Hegna, J. D. Callen, and A. H. Kritz, *Phys. Plasmas* **16**, 102505 (2009).
- ¹⁸F. S. B. Anderson, A. F. Almagri, D. T. Anderson, P. G. Mathews, J. N. Talmadge, and J. L. Shohet, *Fusion Technol.* **27**, 273 (1995).
- ¹⁹J. M. Canik, D. T. Anderson, F. S. B. Anderson, K. M. Likin, J. N. Talmadge, and K. Zhai, *Phys. Rev. Lett.* **98**, 085002 (2007).
- ²⁰S. P. Gerhardt, J. N. Talmadge, J. M. Canik, and D. T. Anderson, *Phys. Plasmas* **12**, 056116 (2005).
- ²¹T. Rafiq and C. C. Hegna, *Phys. Plasmas* **13**, 062501 (2006).
- ²²S. I. Braginskii, *Rev. Plasma Phys.* **1**, 205 (1965).
- ²³J. W. Connor and R. J. Hastie, *Plasma Phys. Controlled Fusion* **27**, 621 (1985).
- ²⁴J. W. Connor, R. J. Hastie, and J. B. Taylor, *Phys. Rev. Lett.* **40**, 396 (1978).
- ²⁵C. C. Hegna and S. R. Hudson, *Phys. Rev. Lett.* **87**, 035001 (2001).
- ²⁶M. Persson, J. L. V. Lewandowski, and H. Nordman, *Phys. Plasmas* **3**, 3720 (1996).
- ²⁷T. Rafiq, J. Anderson, M. Nadeem, and M. Persson, *Plasma Phys. Controlled Fusion* **43**, 1363 (2001).
- ²⁸S. P. Hirshman and O. Betancourt, *J. Comput. Phys.* **96**, 99 (1991).
- ²⁹J. Nührenberg and R. Zille, in *Theory of Fusion Plasmas*, edited by A. Bondeson, E. Sindoni, and F. Troyon (Editrice Compositori, Varenna, 1988), p. 3.
- ³⁰A. H. Boozer, *Phys. Fluids* **25**, 520 (1982).
- ³¹W. D. D'Haeseleer, W. N. G. Hitchon, J. D. Callen, and J. L. Shohet, *Flux Coordinates and Magnetic Field Structure* (Springer-Verlag, Berlin, 1991).
- ³²R. L. Dewar and A. H. Glasser, *Phys. Fluids* **26**, 3038 (1983).
- ³³T. Rafiq and C. C. Hegna, *Phys. Plasmas* **12**, 112505 (2005).
- ³⁴D. T. Anderson, A. Abdou, A. F. Almagri, F. S. B. Anderson, J. M. Canik, W. Guttenfelder, C. Lechte, K. M. Likin, H. Lu, S. Oh, P. H. Probart, J. Radder, V. Sakaguchi, J. Schmitt, J. N. Talmadge, K. Zhai, D. L. Brower, and C. Deng, *Fusion Sci. Technol.* **50**, 171 (2006).
- ³⁵J. Weiland and A. Hirose, *Nucl. Fusion* **32**, 151 (1992).